

Length-scale-dependent cracking and buckling behaviors of nanostructured Cu/Cr multilayer films on compliant substrates

K. Wu, J.Y. Zhang, J. Li, Y.Q. Wang, G. Liu *, J. Sun *

State Key Laboratory for Mechanical Behavior of Materials, Xi'an Jiaotong University, Xi'an 710049, China

ARTICLE INFO

Article history:

Received 21 May 2015

Revised 16 August 2015

Accepted 22 August 2015

Available online 5 September 2015

Keywords:

Nanostructured multilayer films

Cracking and buckling behaviors

Adhesion energy

Deformation mechanism

Length scale effect

ABSTRACT

Cu/Cr nanostructured multilayer films (NMFs) with modulation periods (λ) ranging from 250 nm to 10 nm and modulation ratios (η) ranging from 0.1 to 2.0 were prepared on flexible polyimide substrates by using magnetron sputtering. Upon uniaxial tensile testing, the critical cracking strain (ε_c), critical buckling strain (ε_b), and fracture toughness (K_{IC}) of the NMFs were experimentally measured and all of the mechanical properties showed remarkable λ - and η -dependences. The cracking and buckling behaviors of the Cu/Cr NMFs were systematically investigated and both were found to depend strongly on the length scale. Based on an energy balance model, the interfacial adhesion energies (Γ) were determined using the measured buckle dimensions. Cracking maps and buckling maps were constructed from the experimental data to summarize the effects of λ and η on the cracking and buckling modes, respectively. In the cracking map, two regimes can be identified: one is brittle fracture with straight cracks and the other is ductile fracture with zigzag cracks. The ductile fracture regime is located in the region where $\lambda \sim 40 \pm 20$ nm and simultaneously $\eta < \sim 0.3$, and the brittle-to-ductile transition is characterized by a fracture toughness criterion of $K_{IC} \sim 12.5$ MPa m^{1/2}. In the buckling map, four regimes are distinguished: cracked rectangular buckles, uncracked rectangular buckles, cracked triangular buckles, and uncracked triangular buckles. The effects of the length-scale-dependent deformation and adhesion energies on the buckling behaviors were discussed. A combined dimensionless parameter of $K_{IC}/\sqrt{E_f\Gamma}$ (E_f : elastic modulus of the NMF) was proposed to assess the buckling behaviors, and the $K_{IC}/\sqrt{E_f\Gamma}$ contours coincided well with the boundaries dividing the four buckling regimes.

© 2015 Acta Materialia Inc. Published by Elsevier Ltd. All rights reserved.

1. Introduction

Flexible substrate-supported metal films have aroused extensive concerns due to their diverse applications in stretchable electronics, such as paper-like electronic displays [1–3], wearable electronics [4] and prosthetic skin [5,6]. To maintain high levels of performance, reliability, and integrity, flexible electronic devices are required to endure large stretching, compressing, twisting or other deformations. Cracking and buckling represent the two major mechanical failure mechanisms of metal film/polymer substrate structures, which, because they lead to a loss of properties and even catastrophic failure, should be avoided in applications. However, buckling can also be exploited as a useful tool in many novel measurement methods [7–11], especially in determining internal stress [12], adhesion energy [13,14] and elastic modulus [15] of the metal thin films that are hardly measured using

conventional methods applicable to their bulk counterparts. Therefore, understanding the cracking and buckling behaviors appears to be crucial for metal film/polymer substrate systems.

Over the recent decades, extensive experimental and theoretical studies have been performed to investigate the buckling behaviors of films on rigid substrates [16–19]. Three typical buckling modes, i.e., straight-sided buckle, varicose buckle and telephone cord buckle, and the transition in these modes were studied in the framework of the Föppl-von Kármán (FvK) theory of thin plates. Recently, the scope of buckling research has been expanded dramatically to the films deposited on compliant substrates, driven by the rapid development of stretchable electronics. Some limited methods, including bending tests [20,21], compressive tests [22,23] and tensile tests [24–28], have been developed to investigate the buckling behaviors of brittle films on compliant substrates. In general, the bending test involves a simple mechanical bending device with relatively low measurement precision. The compressive test is applicable only to systems with substrate thicknesses on the order of a few to tens of millimeters. In comparison, the uniaxial tensile test is the most commonly used and a

* Corresponding authors.

E-mail addresses: lgsammer@mail.xjtu.edu.cn (G. Liu), junsun@mail.xjtu.edu.cn (J. Sun).

more reliable method for studying cracking and buckling behaviors. During uniaxial loading of the brittle film/flexible substrate system, microcracks perpendicular to the loading direction will first be created when the applied strain reaches a critical cracking strain. Further increasing the applied strain, the microcrack density will increase to a plateau. Thereafter, buckling of the film strips will form, driven by the compressive stress transverse to the tensile direction due to the mismatch in Poisson's ratio between the hard film and soft substrate.

A large amount of work [21,24,25,29–34] dealing with the failure mechanism of compliant substrate-supported hard thin films has suggested that the cracking and buckling behaviors are complex and influenced by many factors, such as stress state, film thickness and film/substrate interfacial adhesion. For example, buckling behaviors in the polymer-supported Si_3N_4 films were reported [20] to evolve from straight-sided buckles to circular ones upon increasing the external compressive strain. A similar transition from straight-sided to circular buckles was observed [22] in the Ni film/polycarbonate substrate system, which was related to the release of external compressive stress. Some studies have demonstrated that the buckle shapes and dimensions are highly dependent on the film thickness. In the polyimide-supported Cr films, the buckle dimensions increased with the film thickness, and the buckle shape changed from rectangular to triangular when the film thickness was greater than approximately 100 nm [13]. In the polyimide-supported thin indium tin oxide films, buckles in the 100-nm-thick film cracked at the top while those in the 80-nm-thick film were free of cracking [35], even under the same experimental conditions. It was also demonstrated [28] that, when increasing the film thickness of diamond-like carbon film, the critical buckling strain decreased, but the area of a single buckle patch increased. In addition, the buckling process is affected by film/substrate interfacial adhesion. Under the same film thickness, the stronger the interfacial adhesion, the higher the critical buckling strain and the smaller the buckles [36]. Moreover, recent results have strongly suggested that plasticity may also be involved in the buckling process, although previous studies on thin film buckling had usually been based on the theoretical framework of elastic mechanics. In experiments, plastic folding was observed [37] around buckling structures on gold films, which modified the buckling patterns remarkably. From molecular dynamic simulations, it was revealed [38,39] that dislocations could be nucleated and emitted from specific regions of the metal films during the buckling process, leading to significant plastic deformation in buckled structures such as straight sided buckles. These results suggest that the buckling behaviors should be associated with the mechanical properties and deformation behaviors of the films.

However, the aforementioned studies were, without exception, focused on single layer films. Similar investigations have seldom been reported for nanostructured multilayer films that are adherent to compliant substrates. Metallic nanostructured multilayer films (NMFs) have many potential applications due to their promising mechanical properties and significant theoretical interest [40–45]. Microstructures of the NMFs are characterized by (i) alternating nanoscale layers of two different single-phase metals (modulation structure) and (ii) a large number of interfaces. The effects of the length scale and constitutive phases on the mechanical properties of the NMFs, such as hardness, strength, ductility, and toughness, have been experimentally investigated [46–53]. Some strengthening models have been proposed (refer to Ref. [46] and the references therein) to account for the length-scale-dependent hardness/strength, and a micromechanical model has been recently developed [50] to describe the deformation behaviors of the NMFs. From these experiments and models, it is clear that the mechanical properties and deformation

behaviors of the NMFs are controlled by the modulation structure (modulation period and modulation ratio), which, for single layer films, should affect the cracking and buckling behaviors. However, the cracking and buckling behaviors of metallic NMFs are poorly understood at present, and their dependence on the modulation structure is still unclear.

In this paper, we report systematic experiments to determine the effects of the modulation structure and mechanical properties on the cracking and buckling behaviors of NMFs. For this purpose, polyimide-supported fcc/bcc-type Cu/Cr NMFs are chosen as the studied materials that are tailored over wide ranges of both modulation period (λ) and modulation ratio (η). The mechanical properties are measured as a function of the modulation structure, and the buckle dimensions are measured after stretching, which are utilized to quantitatively estimate the adhesion energies of the film/substrate system. The cracking and buckling behaviors will be discussed with respect to the modulation structure, mechanical properties and interfacial bonding, and finally, failure maps will be developed.

2. Experimental procedures

2.1. Materials

Cu/Cr NMFs with different modulation periods λ ($\lambda = h_{\text{Cu}} + h_{\text{Cr}}$, h_{Cu} : thickness of the Cu layers, and h_{Cr} : thickness of the Cr layers) and modulation ratios η ($\eta = h_{\text{Cr}}/h_{\text{Cu}}$) were deposited on 125 μm thick polyimide substrates and Si (111) substrates, respectively, via direct current magnetron sputtering at room temperature. The films on the polyimide substrates were used for tensile testing, while those on the Si substrates were used for residual stress measurement. The purities of the Cu and Cr targets were 99.999% and 99.95%, respectively. The base pressure was $\sim 5 \times 10^{-8}$ Torr prior to sputtering and the processing pressure was $1.0\text{--}3 \times 10^{-3}$ Torr using pure Ar gas during deposition. To manifest the length scale effect clearly, λ and η of the NMFs are changed independently. Two different series of samples were prepared. One series of NMFs have a constant modulation ratio of $\eta = 1.0$, but a wide modulation period range λ from approximately 10 to 250 nm. The other ones have a constant λ ($\lambda = 10, 25, 50$ and 100 nm, respectively), but a wide range of η from 0.1 to 2.0. The total film thickness of all of the NMFs was fixed to approximately 1000 nm. During deposition, the first layer directly on the polyimide substrate was always Cr and the topmost layer was always Cu. Without breaking vacuum, all of the as-deposited NMFs were annealed at 150 °C for 2 h to stabilize the microstructure and eliminate the residual stress. For comparison, single-layered Cu and Cr films with thickness from approximately 30 to 250 nm were also deposited on the polyimide and Si substrates, respectively, following the same preparing technology and treatments.

2.2. Microstructure characterization

X-ray diffraction (XRD) experiments were carried out using an improved Rigaku D/max-RB X-ray diffractometer with Cu K α radiation and a graphite monochromator to determine the crystallographic texture. The residual stress measurements were performed using the substrate curvature method [54–57]. High-resolution transmission electron microscopy (HRTEM) observations were performed to observe the modulated structure and interfaces using a JEOL-2100F TEM. Atomic force microscopy (AFM) was applied to examine the film surface roughness using a Bruker Dimension Icon.

2.3. Uniaxial tensile testing

Uniaxial tensile testing was performed on a Micro-force Test System (MTS® Tytron 250) at a constant strain rate of $1 \times 10^{-3} \text{ s}^{-1}$ at room temperature. All of the samples have a gauge section of 30 mm in length and 4 mm in width. During tensile testing, the force and displacement were automatically recorded by a machine and a high-resolution laser detection system, respectively, which can be subsequently converted into stress-strain curves for the NMFs [50,58–60]. The yield strength (σ_y) is determined as the 0.2% offset. A critical macroscopic cracking strain (ε_c), characterizing the microcrack formation at the microscopic level rather than rupture strain or elongation, can be used to represent the deformation capability or ductility for this type of films. Tensile tests combined with the electrical resistance change method (ERCM) was most recently developed to determine in situ the critical cracking strain ε_c of the polymer-supported NMFs with simple performance but precise measurement [50,60]. The fracture toughness (K_{IC}) was subsequently calculated, following the method given in our previous publications [50,58,59]. The critical buckling strains, ε_b , were measured by examining the film surfaces stretched to different strains and finding the critical point where buckles were nucleated.

2.4. Observations and measurement of cracks and buckles

Scanning electron microscopy (SEM) was used to observe ex situ the morphologies of cracks and buckles. Atomic force microscope (AFM) experiments were performed at room temperature to determine the buckle dimensions, including the buckle heights and widths. The width and height of a buckle were averaged on at least three measurements at different positions of the buckle. In addition, a minimum of 200 buckles was measured for each NMF to obtain average buckle dimensions. Because the triangular buckles change in dimension along the tensile direction, three measurements at different buckle positions were taken, respectively. Buckles with large crack openings at the top and/or base were excluded from the statistics used for interfacial energy calculation. To analyze the interfacial failure mechanism and ensure that the multilayers/substrate interface had failed, some NMF buckles were cross-sectioned and characterized using dual beam focused ion beam/scanning electron microscopy (FIB/SEM) using an FEI microscope (results not presented here).

3. Results

3.1. Microstructure

The XRD spectra of Cu/Cr NMFs revealed a strong $<111>$ out-of-plane texture in the fcc Cu layers and a strong $<110>$ out-of-plane texture in the bcc Cr layers (Fig. 1). The in-plane orientations are random in both of the constituent layers.

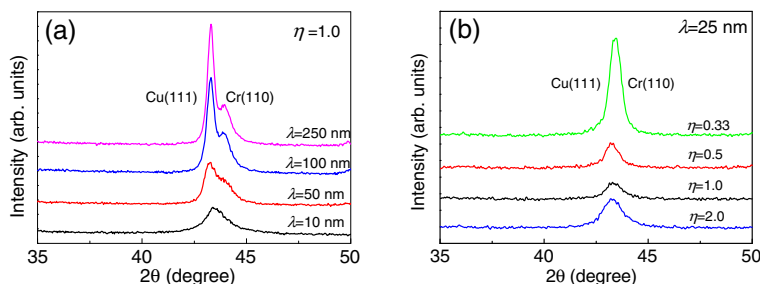


Fig. 1. XRD spectra of the Cu/Cr NMFs with different λ (a) and different η (b).

The measured residual stresses of the single-layer Cu and Cr films and Cu/Cr NMFs are shown in Fig. 2(a)–(c), where all of the single-layer Cu or Cr films and multilayers exhibit tensile residual stresses. The tensile residual stresses may be generated due to an island coalescence mechanism [61–65], where neighboring grains in the growing film are presumed to spontaneously join together under the action of interatomic forces, eliminating two free surfaces in favor of an elastically strained grain boundary. Both of the residual stresses in the single-layer Cu and Cr films decrease with increasing films thickness. However, the Cr films display residual tensile stresses that are much greater than those in the Cu films. The residual stress in the multilayers decreases with increasing modulation period, which changes slightly with modulation ratio. Generally, the residual stress in the Cu/Cr multilayers is between those of the single-layer Cu films and Cr films, and seems to arise primarily from the Cr layers, which is similar to the results of Misra et al. [55]. There have been many reports [55,66–71] on the growth-induced residual stress in sputtered Cr films, claiming that the residual stress is dependent not only on the film thickness but also on the deposition technologies such as deposition rate, temperature and Ar pressure. The residual stress in the present single-layer Cr and multilayer Cu/Cr films is much lower than that in Misra et al.'s work [55], which should be associated with the differences in preparation technologies, including the deposition parameters and annealing treatments [68,71–73].

Here, we should mention that the measurements of residual stress in the Cu or Cr layers were based on their single layer films in the present work. Some new experimental approaches, e.g., synchrotron X-ray diffraction [74–76], have been recently developed to precisely measure in situ the stresses in the constituent layers of the metal NMFs. These advances will definitely help us to deeply understand the stress distributions within the NMFs in the future.

Representative cross-sectional TEM images of some Cu/Cr NMFs were displayed in Fig. 3(a)–(d), where one can see clear modulated layer structures with columnar grains in the Cu layers and ultrafine nanocrystals in the Cr layers. No significant intermixing has been observed between the Cu and Cr layers, as indicated by the interfacial HRTEM (Fig. 3(e) and (f)). In addition, the Cr/substrate interfaces are clear and independent of the modulation period and modulation ratio. Measurements of surface roughness show that the average root mean square (RMS) roughness are in the range 2.0–4.0 nm, which has a negligible influence on the cracking and buckling behaviors.

3.2. Mechanical properties

The yield strength (σ_y), critical cracking strain (ε_c), and fracture toughness (K_{IC}) of the NMFs with different η and λ were experimentally determined and summarized in Table 1. At $\eta = 1.0$, σ_y monotonically increases with decreasing λ . ε_c and K_{IC} first increase and then decrease, leaving a maximum value with a critical modulation period of ~ 50 nm. The increase in σ_y mainly originates

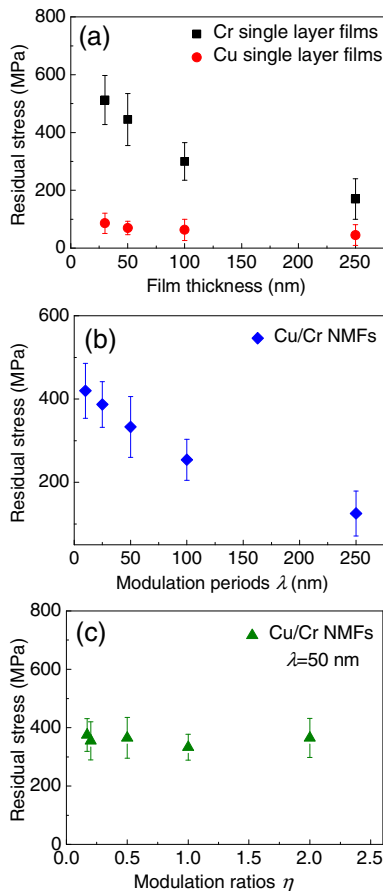


Fig. 2. (a) Evolution of tensile residual stress with film thickness in single layer Cu films and Cr films. Evolution of residual stress in Cu/Cr NMFs as a function of modulation period λ (b) and modulation ratio η (c), respectively.

the interfacial strengthening, according to Misra et al.'s model [46]. The unexpected change in ε_c and K_{IC} with λ can be explained by a constraint effect that is exerted by the relatively soft Cu layers on the brittle microcrack-initiating X layers. Details about the underlying mechanisms can be found in our previous paper [59] and are not repeated here.

At a constant λ , σ_y decreases while ε_c and K_{IC} increases monotonically with decreasing η , which are similar to our previous reports on Cu/Nb and Cu/Zr NMFs [50]. These evolution trends can be well explained because a small η means an increase in the soft Cu layers that will promote the deformation.

3.3. Length-scale-dependent cracking behavior

Cracks in the Cu/Cr NMFs evolved with the applied loading. At low strains, short primary cracks nucleated in the film once the applied strain exceeds the critical cracking strain ε_c and grew perpendicularly to the loading direction. Upon further stretching, the existing cracks propagated further, and new cracks nucleated between the existing cracks. The crack density increased with applied strain until it reached a plateau of approximately 17–30%.

The crack morphology was strongly dependent on both the modulation period, λ , and the modulation ratio, η . Fig. 4(a)–(i) shows representative SEM images of the crack pattern in the 10%-stretched NMFs with different λ ($\lambda = 25$ nm, 50 nm, and 100 nm) and different η ($\eta = 0.1, 1.0$, and 2.0). The NMFs display a cleavage-like fracture morphology and the cracks are highly straight when η is relatively high, i.e., ≥ 1.0 , regardless of λ

(Fig. 4(d)–(i)). This result suggests that the cracks, once nucleated, instantly traverse the entire width and thickness of the NMFs. When η is reduced to 0.1, however, the cracks can be either straight at large λ (e.g., $\lambda = 100$ nm as in Fig. 4(c)) or zigzag at small λ (e.g., $\lambda = 25$ nm as in Fig. 4(a)). A brittle-to-ductile transition is found when λ decreases from 50 nm (Fig. 4(b)) down to 25 nm, indicative of significant length-scale-dependent cracking behaviors.

All of the experimental results on the crack morphology are summarized in Fig. 4(j) from which a cracking map with λ and η as the axes can be constructed. Two regimes are clearly identified in this figure. One has a semi-elliptical shape and is located within $\lambda = \sim 40 \pm 20$ nm and simultaneously $\eta < \sim 0.3$; in this region, the NMFs display zigzag cracks (ZC). The other one covers the remaining area, where the NMFs display straight cracks (SC). This cracking map implies that the ductile fracture with zigzag cracks occurs only when the NMFs have a relatively higher critical cracking strain, refer to Table 1 in which ε_c reaches a maximum value at λ close to ~ 50 nm ($\eta = 1.0$) and is also remarkably enhanced by reducing η , especially below ~ 0.3 .

3.4. Length-scale-dependent buckling behavior

3.4.1. Buckle morphology

As the film fragmented, buckles were subsequently produced perpendicular to the channel cracks when further increasing the tensile strain over approximately 14%. Fig. 5(a)–(c) shows fracture patterns of Cu/Cr NMFs with different λ (25, 50, and 100 nm) at a constant $\eta = 1.0$, stretched to approximately 28% strain. In addition to cracks, buckles are clearly observed, as indicated by the arrows. All of the buckles are a rectangular in shape, which is indicative of a rectangular buckle footprint, and the buckles cracked at the apex and even at the base. In the case of η fixed as 1.0, the buckle morphology is insensitive to λ . When λ is fixed to 25 nm (Fig. 5(d)–(f)) or 50 nm (Fig. 5(g)–(i)); however, the buckle morphology is found to evolve with η . At $\eta = 2.0$, the buckles in the two NMFs are rectangular with crack (Fig. 5(f) and (i)). When η is reduced to 0.3, the buckles in the $\lambda = 25$ nm NMFs are still rectangular but all are free of cracks (Fig. 5(e)). While in the $\lambda = 50$ nm NMFs, cracked and uncracked buckles coexist with the same rectangular shape (Fig. 5(h)). When further reducing η to 0.1, the buckle shape fully changed from rectangular to triangular. All of the triangular buckles are uncracked in the $\lambda = 25$ nm NMFs (Fig. 5(d)) but some are cracked in the $\lambda = 50$ nm ones (Fig. 5(g)). These results mean that the buckle morphology is highly dependent on both λ and η , and their interplay.

The experimental results on the buckle morphology are summarized in Fig. 5(j) from which a buckling map with λ and η as the axes can be similarly constructed. More complex than the cracking map, the buckling map can be divided into four regimes. In these four regimes, the buckles are (i) rectangular and cracked (RC), (ii) rectangular and uncracked (RUC), (iii) triangular and cracked (TC), and (iv) triangular and uncracked (TUC). At $\lambda \leq 10$ nm or $\lambda \geq 100$ nm, the buckles will be rectangular and cracked regardless of η . While at $\eta \geq 0.5$, the buckles will be rectangular and cracked regardless of λ . The regimes with triangular buckles are only located within $\lambda = \sim 40 \pm 30$ nm and simultaneously $\eta < \sim 0.3$, which is slightly larger than the ductile fracture regime revealed in the cracking map (Fig. 4(j)). The evolution in buckle morphology is related to the length-scale-dependent deformation behavior, which will be discussed later.

3.4.2. Critical buckling strain and buckle parameters

The critical buckling strain, ε_b , is plotted in Fig. 6(a) as a function of λ (at $\eta = 1.0$) and in Fig. 6(b) as a function of η (at $\lambda = 25$ and 50 nm). In Fig. 6(a), ε_b changes slightly when $\lambda < \sim 50$ nm, but

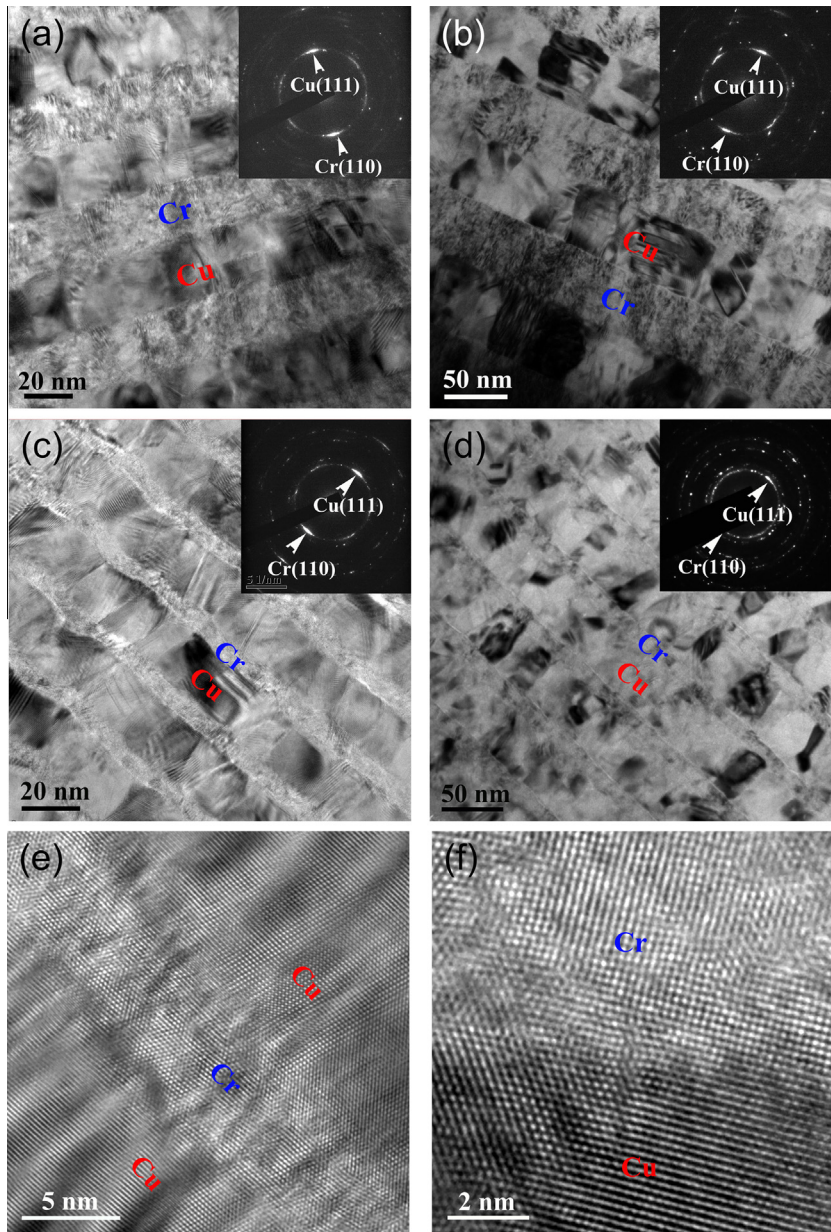


Fig. 3. Bright-field cross sectional TEM micrographs showing the microstructure of $\eta = 1.0$ Cu/Cr NMFs with $\lambda = 50$ nm (a) and $\lambda = 100$ nm (b), $\eta = 0.3$ Cu/Cr NMFs with $\lambda = 25$ nm (c) and $\lambda = 50$ nm (d). The insets show the corresponding selected area diffraction patterns. (e) and (f) are HRTEM images typically showing the clear Cu/Cr interfaces.

sharply increases at $\lambda = 100$ nm. When λ reaches 250 nm, no buckles will be formed even if stretched to $\sim 30\%$. In Fig. 6(b), ε_b is strongly η -dependent when $\eta \leq \sim 0.3$, and insensitive to η when $\eta > \sim 0.3$.

With the NMFs stretched to approximately 28%, the buckle dimensions and area fraction of the buckles were statistically measured. Fig. 6(c) shows the dependence of the buckle dimensions (buckle width and buckle height) on λ at $\eta = 1.0$. Comparing Fig. 6(c) with (a), the λ -dependence of the buckle dimensions is similar to that of ε_b . This result indicates that a critical point exists at $\lambda = \sim 50$ nm, below which the evolution of the buckle dimensions with λ is inconspicuous, while above that value the buckle dimensions increase greatly. Likewise, the η -dependence of the buckle dimensions is close to that of ε_b , see Fig. 6(d) compared with (b). The area percentage of buckles, however, exhibits λ dependence

(Fig. 6(e)) and η dependence (Fig. 6(f)) in contrast to that of ε_b . It is difficult to form buckles when $\lambda \geq \sim 100$ nm and/or $\eta < \sim 0.3$.

Previous studies on flexible substrate-supported single-layer films [13,14,27,77] have reported that the buckling behaviors were highly dependent on the film thickness. For example, Tarasovs et al. [24] found that in polyimide substrate-supported single-layer SiN_x films, thicker films have lower critical buckling strains. Similar results were demonstrated by Bernoulli et al. [28] on diamond-like carbon films and by Jin et al. [27] on Cr films; in these studies the critical buckling strain decreased with increasing film thickness. Here, in the present NMFs that have the same thickness, the buckle morphology, dimensions and onset strains vary with the modulation structure (λ and η) rather than the film thickness because the modulation structure dominates the scale-dependent deformation in the NMFs, which will be discussed later.

Table 1Summary of mechanical properties of Cu/Cr NMFs with different modulation structure at a strain rate of 10^{-3} .

Modulation periods (nm)	Modulation ratios	Yield strength (MPa)	Critical cracking strain (%)	Fracture toughness (MPa m ^{1/2})	Adhesion energy (J m ⁻²)
10	0.1	1292 ± 105	0.7 ± 0.06	6.0 ± 0.4	5.5 ± 0.4
	0.3	1310 ± 100	0.6 ± 0.05	4.5 ± 0.3	5.0 ± 0.2
	1.0	1325 ± 112	0.6 ± 0.04	3.1 ± 0.2	5.1 ± 0.3
25	0.1	745 ± 43	3.0 ± 0.15	14.2 ± 1.2	6.8 ± 0.5
	0.2	868 ± 55	2.7 ± 0.16	13.0 ± 1.0	6.7 ± 0.5
	0.3	1075 ± 68	2.1 ± 0.11	10.6 ± 0.8	5.6 ± 0.4
	0.5	1142 ± 75	1.4 ± 0.10	8.0 ± 0.7	5.2 ± 0.3
	1.0	1345 ± 86	1.1 ± 0.09	6.5 ± 0.6	5.1 ± 0.3
	2.0	1480 ± 102	1.0 ± 0.08	5.7 ± 0.6	5.3 ± 0.3
50	0.1	510 ± 30	2.5 ± 0.15	13.4 ± 1.0	7.5 ± 0.6
	0.2	610 ± 36	2.4 ± 0.12	12.4 ± 0.9	6.9 ± 0.5
	0.3	750 ± 55	2.0 ± 0.11	10.4 ± 0.6	6.4 ± 0.5
	0.5	930 ± 74	1.8 ± 0.11	8.6 ± 0.5	5.5 ± 0.4
	1.0	1270 ± 86	1.5 ± 0.10	7.7 ± 0.4	5.2 ± 0.3
	2.0	1444 ± 100	1.2 ± 0.06	6.9 ± 0.3	5.3 ± 0.3
100	0.1	450 ± 36	1.9 ± 0.12	11.6 ± 0.9	55.0 ± 8.0
	0.3	600 ± 49	1.5 ± 0.09	9.0 ± 0.6	50.0 ± 6.0
	1.0	1045 ± 85	1.2 ± 0.08	6.7 ± 0.5	49.0 ± 4.0
250	1.0	811 ± 55	1.0 ± 0.08	5.0 ± 0.4	N/A

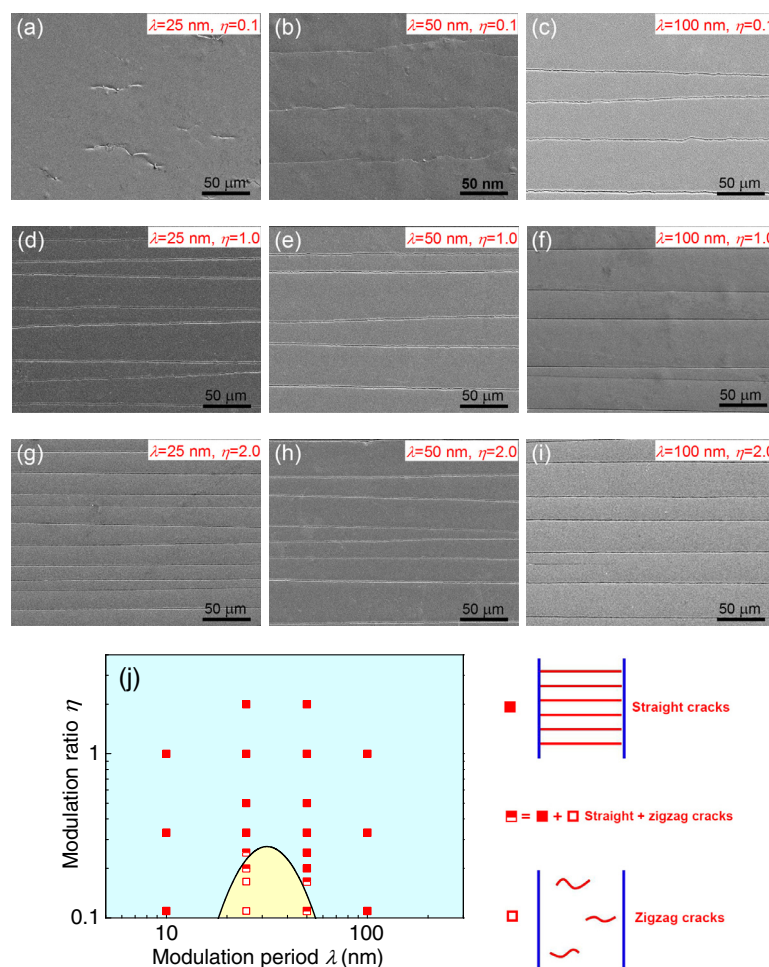


Fig. 4. Representative SEM images showing the crack morphologies of $\eta = 0.1$ Cu/Cr NMFs with $\lambda = 25$ nm (a), $\lambda = 50$ nm (b), and $\lambda = 100$ nm (c), $\eta = 1.0$ Cu/Cr NMFs with $\lambda = 25$ nm (d), $\lambda = 50$ nm (e), and $\lambda = 100$ nm (f), and $\eta = 2.0$ Cu/Cr NMFs with $\lambda = 25$ nm (g), $\lambda = 50$ nm (h), and $\lambda = 100$ nm (i) strained to 10%. (j) Cracking map for Cu/Cr NMFs constructed from experimental data. The experimental observations are summarized with symbols: straight cracks (solid squares), straight + zigzag cracks (half squares) and zigzag cracks (open squares).

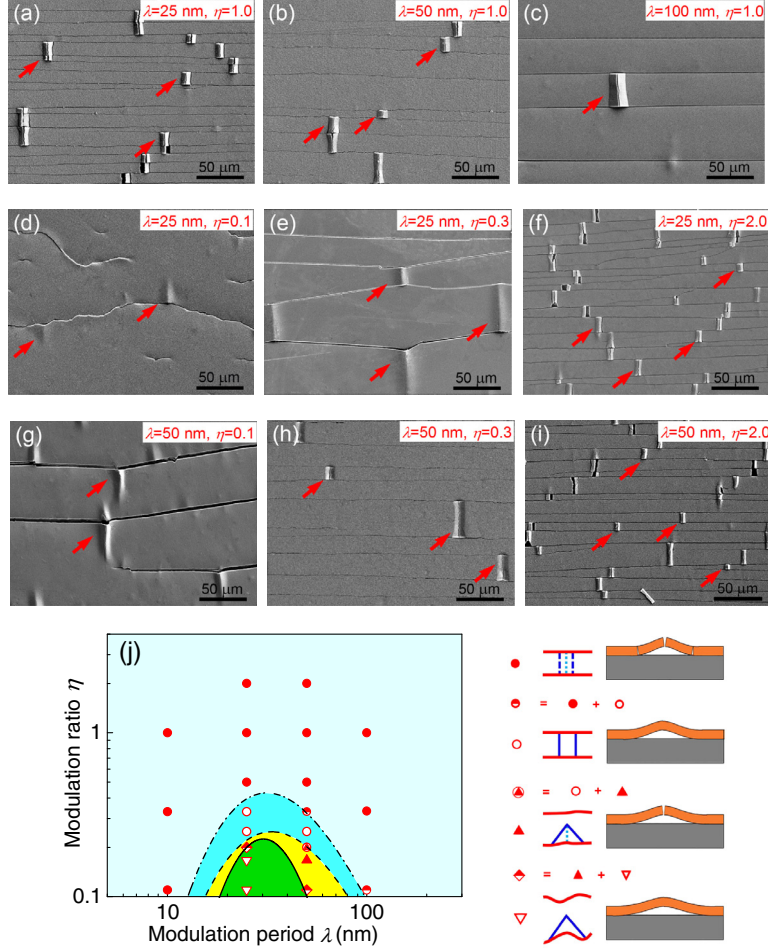


Fig. 5. Representative SEM images showing the buckle morphologies of $\eta = 1$ Cu/Cr NMFs with $\lambda = 25 \text{ nm}$ (a), $\lambda = 50 \text{ nm}$ (b), and $\lambda = 100 \text{ nm}$ (c), $\lambda = 25 \text{ nm}$ Cu/Cr NMFs with $\eta = 0.1$ (d), $\eta = 0.3$ (e), and $\eta = 2.0$ (f), and $\lambda = 50 \text{ nm}$ Cu/Cr NMFs with $\eta = 0.1$ (g), $\eta = 0.3$ (h), and $\eta = 2.0$ (i) strained to 28%. (j) The buckling map constructed for Cu/Cr NMFs from experimental data. The experimental observations are summarized with symbols: rectangular and cracked buckles (solid circles), rectangular and uncracked buckles (open circles) and triangular and cracked buckles (solid triangles) and triangular and uncracked buckles (open triangles).

3.5. Interfacial adhesion energy between the NMFs and substrate

An energy balance buckle model has been developed by Cordill et al. [13] to determine the adhesion energy of brittle films on flexible polymer substrates, which relates the measured buckle dimensions to the interfacial properties. The functional relation of these quantities is given by

$$\sqrt{\frac{\delta}{h}} = (2\alpha)^{1/4} \frac{l}{h} \left[1 + \sqrt{1 + \frac{3}{4}\alpha \left(\frac{l}{h} \right)^4} \right]^{-1/4} \quad (1)$$

where δ is the buckle height, l is the half buckle width, h is the film thickness and α is a fitted coefficient, which is denoted as

$$\alpha = \frac{4\Gamma(1 - v^2)}{hE_f} \left(\frac{2}{\pi} \right)^4 \quad (2)$$

where Γ is the adhesion energy, v and E_f are the Poisson's ratio and Young's modulus of the film, respectively. Note that this model is applicable for single-layer hard films adherent to flexible substrates, and cannot be directly used in NMFs.

To determine the interfacial adhesion energy between the NMFs and the flexible polymer substrate, we have most recently modified Cordill et al.'s model by incorporating the characteristic modulation parameters of the NMFs [78]. After modification, Eq. (1) is rewritten as

$$\sqrt{\frac{\delta}{\lambda}} = (2\alpha)^{1/4} \frac{l}{\lambda} \left[1 + \sqrt{1 + \frac{3}{4}\alpha \left(\frac{l}{\lambda} \right)^4} \right]^{-1/4} \quad (3)$$

where λ is the modulation period and the other symbols have the same meaning as above. α is revised as

$$\alpha = \frac{4\Gamma(1 - v^2)}{\lambda E_f} \left(\frac{2}{\pi} \right)^4 \quad (4)$$

The modified model has been successfully used to determine the interfacial adhesion energy of polyimide-supported Cu/Zr and Cu/Nb NMFs [78]. Using this modified model for the present Cu/Cr NMFs, the interfacial adhesion energy can be determined based on the buckle dimensions. Fig. 7(a) and (b) present the determined adhesion energy as functions of λ and η , respectively. It is clearly found from Fig. 7(a) that, when $\lambda < \sim 50 \text{ nm}$, the evaluated adhesion energy is λ independent and reaches a constant value of $\sim 5.0 \text{ J m}^{-2}$. However, when $\lambda > \sim 50 \text{ nm}$, the evaluated adhesion energy increases with increasing λ , which is indicative of λ dependence. In Fig. 7(b), a constant value of $\sim 5.0 \text{ J m}^{-2}$ was obtained as the adhesion energy at $\eta > \sim 0.3$, and a similar size effect was found at $\eta < \sim 0.3$; the determined adhesion energy increases with decreasing η . The adhesion energy of $\sim 5.0 \text{ J m}^{-2}$ as determined in the present Cu/Cr NMFs agrees well with the previous report on Cr film/polyimide substrate systems that had an adhesion energy of $\sim 4.5 \text{ J m}^{-2}$ [13].

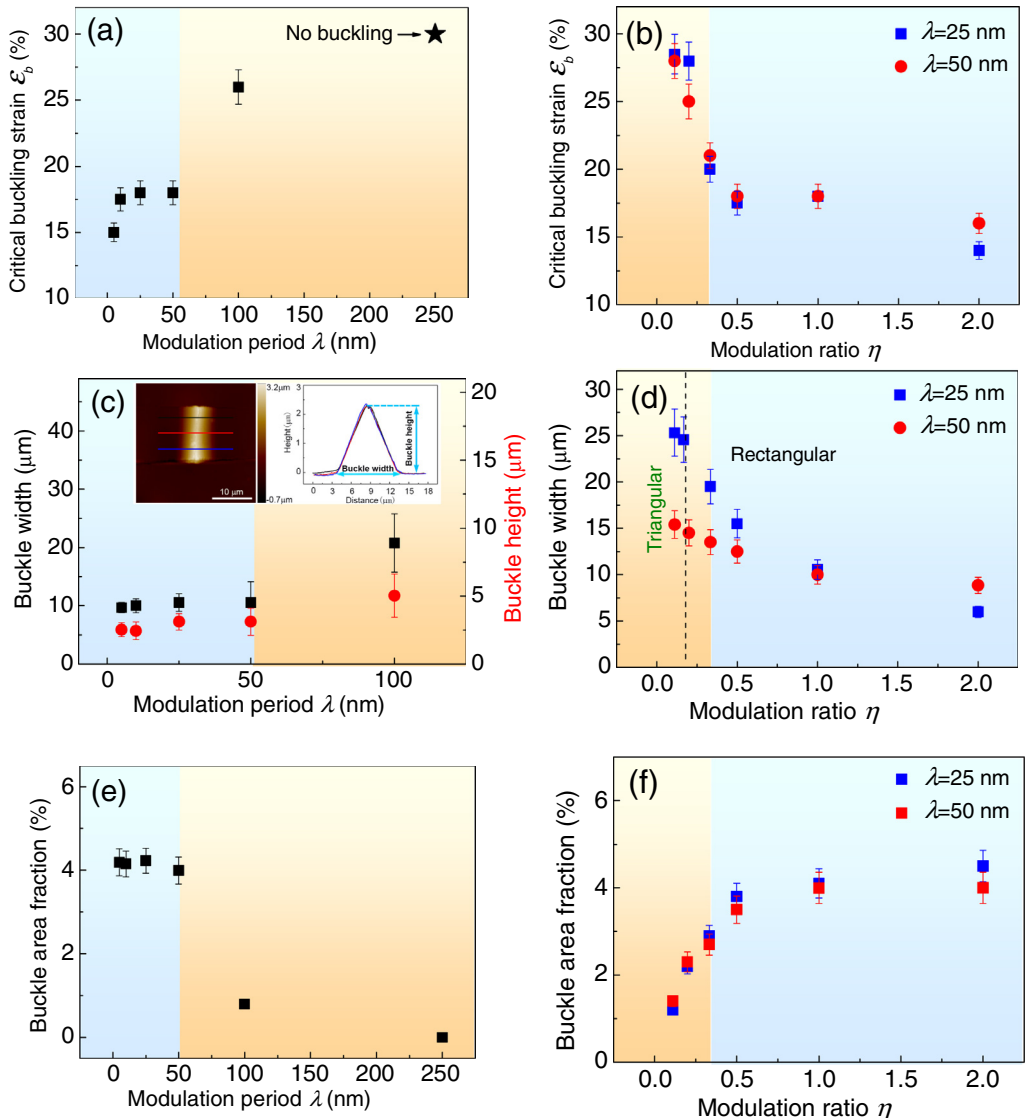


Fig. 6. Dependence of the critical buckling strain ε_b on λ (a) and η (b). Dependence of the buckle width on λ (c) and η (d). Dependence of buckle area fraction on λ (e) and η (f). The insets in (c) are representative AFM images showing a rectangular buckle and corresponding buckle profile illustrating the definition of buckle width and buckle height.

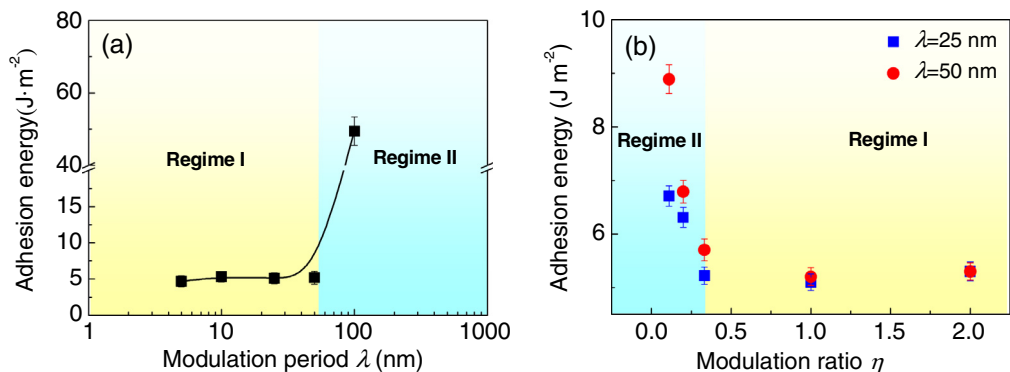


Fig. 7. Variation in adhesion energy with λ (a) and η (b). Two regimes representing length scale-independent and length-scale-dependent ranges, respectively, can be clearly identified.

4. Discussions

In the previous section, we presented experimental results that show that both the cracking and buckling behaviors of the Cu/Cr NMFs are closely dependent on the modulation structure. Cracking and buckling maps, which take λ and η as axes, were constructed. A ductile fracture regime is clearly identified from the cracking map, which locates within narrow λ and η ranges. From the buckling map, four regimes with different buckle morphologies are also distinguished. In this section, the length-scale-dependent deformation and brittle-to-ductile transition will be discussed to understand the cracking behaviors. The buckling behaviors will be analyzed in the context of the film deformation and film/substrate interfacial bonding. In addition, we try to correlate both the cracking and buckling behaviors directly with the mechanical properties of the Cu/Cr NMFs.

4.1. Length-scale-dependent deformation and brittle-to-ductile transition

4.1.1. Modulation period dependence

Many studies (see [46] and the references therein) have been investigated to investigate the effects of the length scale, ranging from micrometers to nanometers, on the deformation behaviors of NMFs, as their characteristic dimensions shrink toward the nanoregime. Some deformation mechanisms have been proposed, e.g., (i) the dislocation pileup (DP) mechanism, which is applicable at length scales of sub-micrometers to a few hundreds of nanometers; (ii) the confined layer slip (CLS) mechanism, which is applicable at length scales of a few to a few hundreds of nanometers, and (iii) the interface barrier crossing (IBC) mechanism, which is applicable at length scales of a few nanometers. The CLS mechanism involves the gliding of a single dislocation loop in the soft phase bounded by two interfaces, while the DP mechanism considers the pileup of dislocations within the thickness space. The thickness of the constituent layers in the present Cu/Cr NMFs is from approximately 8 nm to 125 nm, depending on the modulation structure. This size range falls mainly in the CLS regimes, although a small part may enter the DP regime.

In the case of CLS deformation mechanism, the fracture of the NMFs is predominantly controlled by a constraining effect between the two constituent nanolayers. As in the present Cu/Cr NMFs, the microcracks initiate within and subsequently run across the Cr nanolayers because the harder Cr layers have ductilities lower than their Cu counterparts [59]. Further propagation of the microcracks is arrested by the more ductile Cu layers. Whether the microcracks can be stopped depends on two factors: the first factor is the intensity of the stress/strain fields (ISF) ahead of the microcrack tip. The ISF scales with $\sqrt{h_{Cr}}$ when the size of the crack is approximately h_{Cr} . This behavior would lead to the expectation that a smaller h_{Cr} is favorable for the suppression of crack growth and improved ε_c . The other factor is the shielding of microcrack propagation by plastic deformation (dislocation) activities in the Cu nanolayers, which become rather limited when h_{Cu} is too small. This behavior renders very thin Cu layers less effective in improving ε_c . At $\eta = 1.0$, i.e., $h_{Cr} = h_{Cu} = \lambda/2$, the competition between these two opposing effects leads to the peak in ε_c observed at critical $\lambda_{cri} \approx 50$ nm. Above λ_{cri} , plastic deformation in the Cu layers is not a problem and the ISF is the controlling factor. Reducing h_{Cr} or λ would then promote crack suppression and improve ε_c . Below λ_{cri} , the very thin Cu layers become more and more brittle as they lose the ability to accommodate dislocation activities, weakening the shielding effect of the Cu layers. The microcracks in the Cr layers, although they have small sizes, can now break loose and cause failure. As a result, the ε_c of NMFs decreases with decreasing λ (or h_{Cu}). The

constraining effect between the two constituent nanolayers is the underlying mechanism for the experimentally observed non-monotonic evolution of ε_c with λ . Next, we will try to quantify λ_{cri} based on a micromechanical fracture model and uncover the brittle-to-ductile transition in varying λ .

Hsia et al. [79] have developed a micromechanical model to describe the fracture behavior in laminates consisting of alternating ductile and brittle layers. In their model, the deformation capability of the ductile layers can be quantitatively evaluated by deriving an equilibrium number of dislocations that can accumulate in a single ductile layer. The model assumes that (i) a crack is initially formed in the brittle layers and blocked by an interface and (ii) dislocations are emitted from the crack tip, piled up in the neighboring ductile layer and against the next interface. The cracking of current Cu/Cr NMFs is truly initiated at the brittle Cr layers and blocked by the ductile Cu layer, fitting well with the model. We then employ this model to understand the deformation/fracture mechanisms in the NMFs with $\eta = 1.0$. The dislocations emitted from the crack tip have two competing effects. The first one is that the emitted dislocations blunt the crack tip and thus reduce the tensile stress at the crack tip. The other one is that the dislocations piled up at the interface send a back stress to the crack tip to hinder further dislocation emission. At a given load level, the equilibrium number (n) of dislocations is [79]

$$n = \frac{4\pi(1-\nu)}{\ln(\tilde{\lambda}/\tilde{r})} \left(\frac{\tilde{K}_{app}\sqrt{\tilde{\lambda}}}{A\sqrt{2\pi}} \sin\phi \cos\frac{\phi}{2} - \tilde{\gamma} \right), \quad (5)$$

where ϕ is the angle that the slip plane inclines from the interface (chosen as 45°); A is a factor slightly greater than unity; $\tilde{r} \approx 2.7r_0/b$ with r_0 being the effective core radius and b the Burgers vector of the dislocation in the ductile material; \tilde{K}_{app} , $\tilde{\lambda}$, and $\tilde{\gamma}$ are the normalized values of the far field mode I stress intensity K_{app} (=1.12 $\sigma_{app}\sqrt{\pi\lambda/2}$ [80]), the maximum distance $\lambda_\phi = \lambda/2 \sin\phi$ that the leading dislocation can travel, and the surface energy γ , respectively,

$$\tilde{K}_{app} = \frac{K_{app}}{\mu\sqrt{b}}, \quad \tilde{\lambda} = \frac{\lambda_\phi}{b}, \quad \tilde{\gamma} = \frac{\gamma}{\mu b}, \quad (6)$$

where μ is the shear modulus of the Cu layers. The tensile stress at the blunted crack tip ($\tilde{\sigma}_{tip} = \sigma_{tip}/\mu$) is related to n and \tilde{K}_{app} as

$$\begin{aligned} \tilde{\sigma}_{tip}\sqrt{n} &= 2\sqrt{\frac{2}{\pi}}\tilde{K}_{app} \left(1 - \frac{3(\sin\phi \cos\frac{\phi}{2})^2}{\ln(\tilde{\lambda}/\tilde{r})} \right) \\ &\quad + \frac{12A}{\sqrt{\tilde{\lambda}}\ln(\tilde{\lambda}/\tilde{r})} \tilde{\gamma} \sin\phi \cos\frac{\phi}{2}, \end{aligned} \quad (7)$$

Upon increasing the applied load, further dislocation emission competes with cleavage at the blunted crack tip. When the microcrack tip tensile stress $\tilde{\sigma}_{tip}$ reaches the normalized cohesive strength of the material, $\tilde{\sigma}_c$ ($=\sigma_c/\mu$), cleavage occurs in the ductile Cu layer and the microcrack will propagate and form a through-thickness crack. Under this condition, the far field stress intensity is the fracture toughness of the layered films, i.e., $\tilde{K}_{IC} = \tilde{K}_{app}|_{\tilde{\sigma}_{tip}=\tilde{\sigma}_c}$. Based on this criterion, the maximum number of dislocations emitted from the microcrack tip prior to cleavage (n_{max}) and the normalized fracture toughness (\tilde{K}_{IC}) can be obtained from Eqs. (5) and (7) when reasonable values of $\tilde{\sigma}_c$ (0.3–0.5) are applied to the ductile metals such as Cu. The calculated \tilde{K}_{IC} for Cu/Cr NMFs are shown in Fig. 8(a) as a function of λ . Experimentally measured K_{IC} is also presented in this figure for comparison. Calculations at $\tilde{\sigma}_c = 0.4$ fit well with the

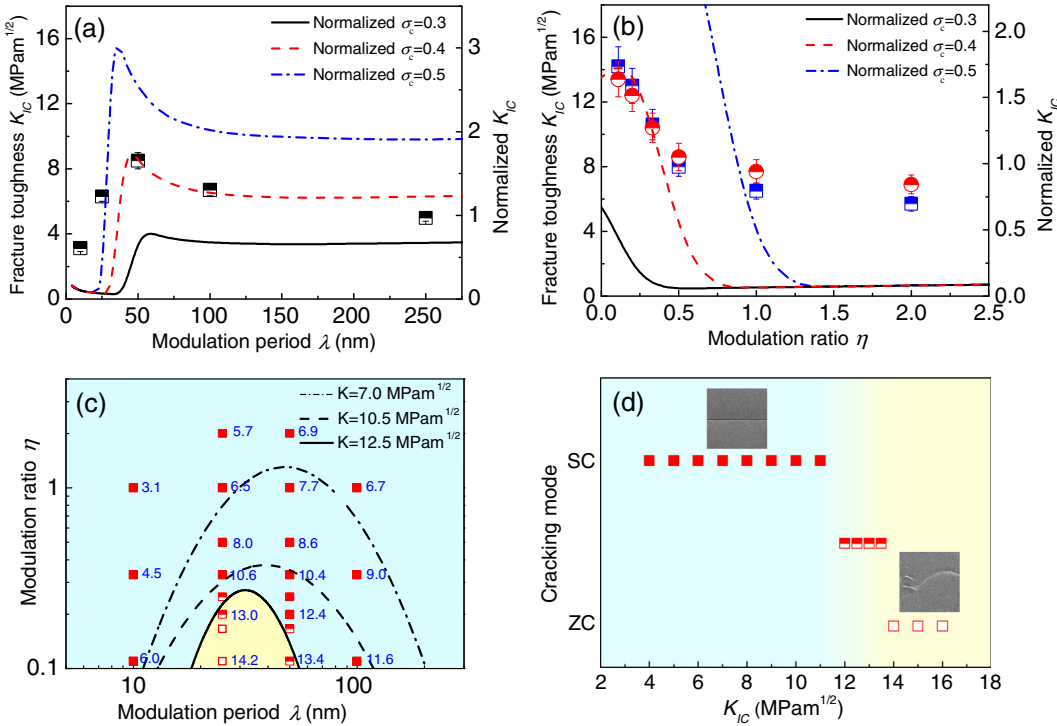


Fig. 8. The dependence of K_{Ic} and the calculated normalized K_{Ic} (lines and right y-axis) on λ (a) and η (b) for the Cu/Cr NMFs. (c) shows experimental K_{Ic} contours as a function of λ and η . (d) Dependence of the buckling mode on K_{Ic} at different λ and η . The insets are corresponding SEM images of cracks showing typically two types of cracking modes, respectively.

measurements, which quantitatively demonstrates the maxima in the fracture toughness at the critical $\lambda_{cri} \approx 50 \text{ nm}$ and clearly manifest the promoted ductile fracture at λ close to λ_{cri} .

4.1.2. Modulation ratio dependence

When λ is fixed, changes in η will induce simultaneous variations in both h_{Cu} and h_{Cr} . Reducing η implies that the thickness of the Cu nanolayers is increased, while those of the Cr layers are correspondingly decreased. At greater η , the NMFs contain higher relative Cr nanolayers contents and show cleavage fractures with straight cracks. Once nucleated in the Cr nanolayers, the microcracks would rapidly traverse the total film thickness and the entire sample width because the thinner Cu nanolayers exert an insufficient shielding effect to block the microcracks. At smaller η , the NMFs are dominated by the Cu nanolayers. Dislocation activities are promoted within the thicker Cu nanolayers. Continuous emission of dislocations from the crack tip can sufficiently reduce the stress/strain at the crack tip, blunt the crack tip substantially, and suppress the cleavage. A ductile fracture is therefore induced in which cracks propagate in a zigzag manner instead of a straight manner. Quantitatively, \tilde{K}_{Ic} can be calculated similarly as a function of η using the above model. As shown in Fig. 8(b), the calculations are in broad agreement with the experimental results, and the trend that the fracture toughness increases with decreasing η is quantitatively demonstrated. In particular, the fracture toughness is greatly improved when η is smaller than ~ 0.3 . This result is consistent with the experimental observations that ductile fracture is favored at η below ~ 0.3 , see Fig. 4(j).

All of the experimental measurements of K_{Ic} of the NMFs are summarized in Fig. 8(c), where K_{Ic} contours can be outlined as a function of λ and η . Comparing Figs. 8(c) and 4(j), the contour of $K_{Ic} = 12.5 \text{ MPa m}^{1/2}$ as the solid line in Fig. 8(c) almost coincides with the boundary that divides the brittle and ductile fracture regimes in Fig. 4(j). The dependence of the fracture mode on K_{Ic} at

different λ and η is further shown in Fig. 8(d), which visually illustrates the fact that the fracture of the present Cu/Cr NMFs, either in a brittle or ductile manner, is predominantly controlled by the intrinsic property K_{Ic} of the films. Due to the constraint effect between the two constituent nanolayers, K_{Ic} of the NMFs is in turn controlled by a synergy between λ and η , not by a single one.

4.2. Effects of deformation and adhesion energy on buckling behavior

4.2.1. Length-scale-dependent adhesion energy

Thickness-dependent adhesion energies have been generally reported for substrate-supported single layer metal films [81–83], where the adhesion energy evaluated using different measurement methods (such as four-point bending, stressed overlayers and indentation tests) was commonly found to increase with increasing film thickness. It has been suggested [84,85] that the plastic energy dissipation in thicker films is responsible for an enhancement of the measured adhesion energy. In this work, the adhesion energy of NMFs, evaluated using the buckling method, is also dependent on the size when λ is greater than approximately 50 nm and/or η is less than approximately 0.3. This behavior will be discussed in light of the deformation mechanisms of the NMFs.

In the above micromechanical model, the maximum number of dislocations emitted from the microcrack tip prior to cleavage (n_{max}) can be calculated from Eq. (5). Fig. 9(a) and (b) depict the evolution of n_{max} with λ (at $\eta = 1.0$) and of η ($\lambda = 25 \text{ nm}$), respectively. In Fig. 9(a), a critical $\lambda \sim 50 \text{ nm}$ is quantitatively identified, below which n_{max} sharply decreases down to a few in magnitude. While beyond this critical point, many more dislocations can accumulate within the Cu nanolayers. This means that the dislocations will be strongly constrained by the interfaces in the regime below $\lambda \sim 50$ and have to glide individually within the in-plane of the Cu nanolayers. Similarly, in Fig. 9(b), a critical $\eta \sim 0.3$ is found, above which the deformation mechanism is CLS.

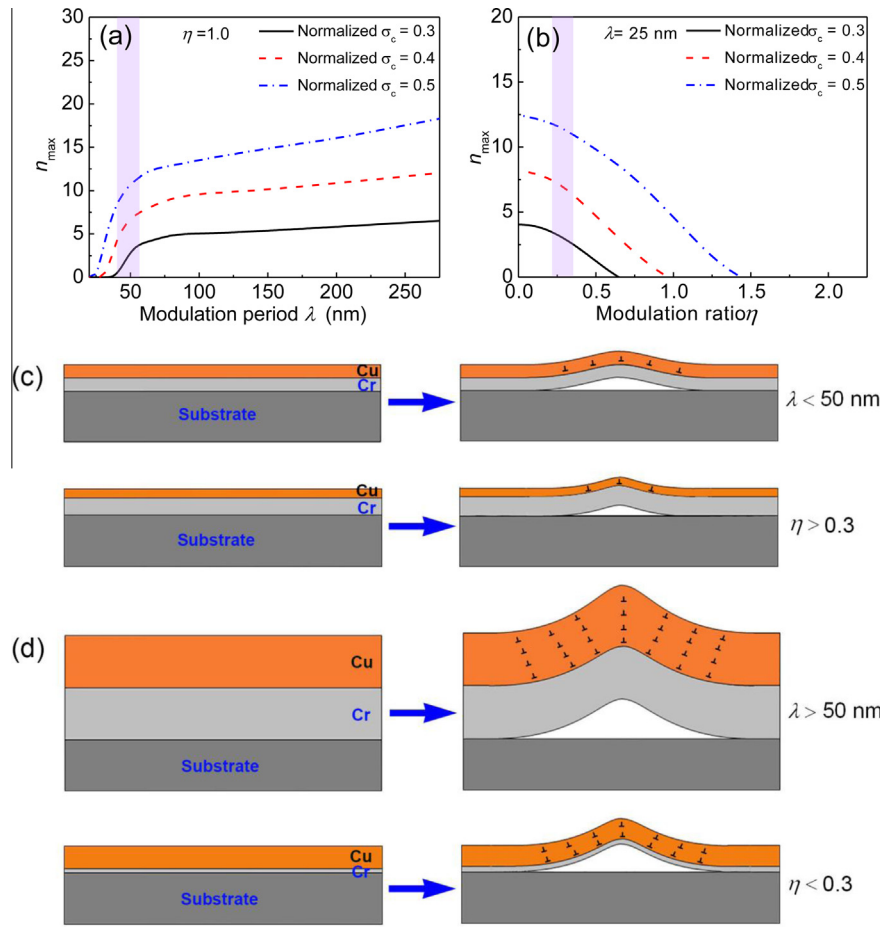


Fig. 9. Dependence of the maximum equilibrium dislocations in the Cu nanolayer on the normalized Cu cohesive strength as functions of λ (a) and η (b). Sketches illustrating the deformation gradient caused by buckling and formation of geometrically necessary dislocations to accommodate the gradient in NMFs with $\lambda < \sim 50 \text{ nm}$ or $\eta > \sim 0.3$ (c) and $\lambda > \sim 50 \text{ nm}$ or $\eta < \sim 0.3$ (d), respectively.

The curvature of the buckles inevitably causes local deformation gradients, for which geometrically necessary dislocations are required to accommodate the deformation discrepancy. At $\lambda < \sim 50 \text{ nm}$ or $\eta > \sim 0.3$ with the CLS deformation mechanism, the induced geometrically necessary dislocations are limited and only single-rows are arrayed in a buckle-like shape (Fig. 9(c)). Therefore, the buckles mainly deform elastically. The determined adhesion energy is λ independent and η independent; both have constant values of $\sim 5.0 \text{ J m}^{-2}$, see regime I in Fig. 7(a) and (b). At $\lambda > \sim 50 \text{ nm}$ or $\eta < \sim 0.3$, the deformation mechanism transits from CLS to DP. The dislocations can now loosely move in both the in-plane and the out-of-plane of the layers. There are broad three-dimensional spaces available for the generation and accumulation of a large number of geometrically necessary dislocations (Fig. 9(d)). The introduction of plastic deformation will overestimate the adhesion energy and result in an enhancement of the determined adhesion energy. The thicker λ is or the smaller η is, the greater the plastic deformation. The remarkable length-scale dependence of the adhesion energy is finally measured and shown as the regime II in Fig. 7(a) and (b).

As a matter of fact, plastic deformation around the interfacial crack tip indeed occurs during the debonding, especially in the NMFs with larger λ and smaller η , which does enhance the practical adhesion energy. Previous studies on single layer films [36,86] suggested that strong interfacial bonding can efficiently enhance the critical buckling strain and reduce the area fraction of the buckles. In the present Cu/Cr NMFs, similar trends were observed when $\lambda > \sim 50 \text{ nm}$ or $\eta < \sim 0.3$ where the increase in adhesion energy was

accompanied with reduced buckle area fraction and enhanced critical buckling strain (Fig. 6). In particular, the critical buckling strain increases almost linearly with the interfacial adhesion energy (Fig. 10(a)), indicating that interfacial bonding plays an important role in the buckling behaviors.

The pronounced effect of interfacial adhesion on the buckling has been highlighted in the flexible substrate-supported brittle single layer films [28,33,36,86–88]. It was generally accepted that buckling is difficult to form at strong interfacial bonding, which means the higher the adhesion energy, the greater the critical buckling strain. However, there were conflicting reports on the evolution of the buckle dimensions with adhesion energy. Kim et al. [36] found that the spalled width decreased with increasing interfacial adhesion for stainless steel-supported diamond-like carbon films. Latella et al. [28] claimed in polycarbonate-supported titania films that poor interfacial adhesion resulted in wider buckles. However, in polyimide-supported Ti films, Taylor et al. [87] observed the opposite phenomenon where strong interfacial adhesion widened the buckles. The discrepancy among these reports implies that the buckle parameters are dependent not only on the interfacial bonding between the films and substrates, but also on the deformation of the films themselves.

4.2.2. Evolution of buckle morphology and parameters

The process of buckle formation can be described as a release of the elastic strain energy stored in the NMFs. From a fracture mechanics point of view, buckling is expected to occur when the elastic energy release rate G exceeds the sum of the adhesion

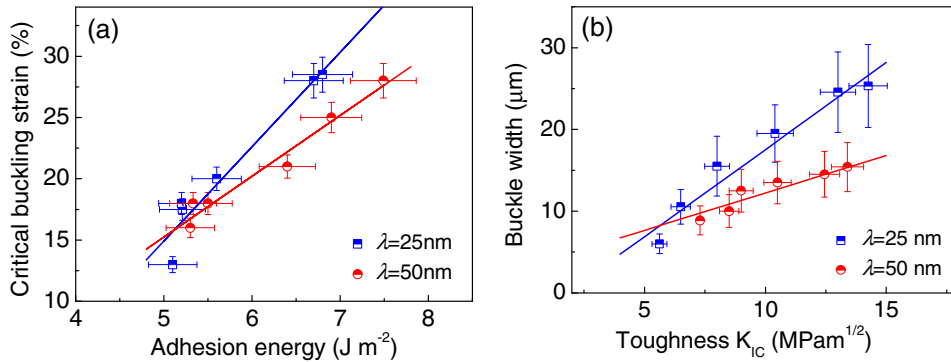


Fig. 10. (a) Scaling relationship between critical buckling strain and adhesion energy. (b) Scaling relationship between buckle width and toughness in Cu/Cr NMFs with $\lambda = 25$ and 50 nm.

energy Γ and plastic dissipation G_p . The curvature of the buckles inevitably causes a local deformation gradient, for which geometrically necessary dislocations are required to accommodate the deformation discrepancy. At $\lambda < \sim 50$ nm or $\eta > \sim 0.3$ with the CLS deformation mechanism, the NMFs buckle elastically and almost no plastic energy dissipation occurs in the buckling process, i.e., $G_p \sim 0$ J m⁻². Upon stretching, debonding began as long as the elastic energy release rate G exceeds the interfacial adhesion energy. Buckling initiated at lower strain and the buckles displayed relatively smaller dimensions. While at $\lambda > \sim 50$ nm or $\eta < \sim 0.3$ with the DP deformation mechanism, a certain number of geometrically necessary dislocations were induced to accommodate the deformation gradient caused by buckling; buckles were therefore initiated at higher applied strain and displayed larger dimensions. Because the maximum number of stored dislocations in the Cu nanolayers is determined by the critical point of fracture, deformation of the NMFs can be properly characterized by K_{IC} . Fig. 10(b) shows a linear correlation between the buckle width and K_{IC} , which indicates that the buckle dimensions rely on the intrinsic properties of the NMFs. At this point, it should be noted that, although a commonly used method for increasing the critical buckling strain is to add adhesion promoters to strengthen the interfacial bonding, the present work shows an alternative way in the NMFs by simply tailoring the modulation structures and concomitantly the deformation behaviors.

The evolution of the buckle morphology is also predominantly related to the length-scale-dependent deformation of NMFs. Because buckling is caused by the lateral compressive stress perpendicular to the tensile direction (x direction), a simple expression as [25,87]:

$$\sigma_y = -v_s \varepsilon E_s + v_f \sigma_x, \quad (8)$$

where ε is the applied strain, E_s is the stiffness of the substrate and v_f is the Poisson's ratio of the film, v_s is a composite term describing the perpendicular contraction of the substrate as a function of the stress parallel to the loading direction and has both elastic and plastic components [87]. The x -axis is parallel to the tensile direction, and the y -axis is perpendicular to the tensile direction. Because a compressive stress gradient is produced from fragment edge to fragment center along the x -axis, the release of strain energy driving buckling will correspondingly decrease toward the fragment center [25]. In the NMFs with slight plastic dissipation as in the case of $\lambda < \sim 50$ nm or $\eta > \sim 0.3$, rectangular footprint buckles will form because a rectangle undertakes the greatest release of strain energy for a given area of film delamination [87]. In the NMFs with appreciable plastic dissipation as in the case of $\lambda > \sim 50$ nm or $\eta < \sim 0.3$, the compressive strain energy in the center of the crack fragment is insufficient to overcome the adhesion energy, leading to a failure mode transition from rectangular buckling to triangular buckling.

The above discussions clearly demonstrated that the buckling behaviors of Cu/Cr NMFs are closely dependent on both the film-/substrate interfacial bonding and the deformation of the film. We use a combined dimensionless parameter, $K_{IC}/\sqrt{E_f \Gamma}$ (E_f is the Young's modulus of the film), to represent the coupling effect of the interfacial bonding and film deformation on buckling. The experimentally derived measurements of $K_{IC}/\sqrt{E_f \Gamma}$ are summarized in Fig. 11(a), where contours can be outlined as a function of λ and η . Refer to the buckling map and four buckling regimes shown in Fig. 5(j), the boundaries dividing the regimes broadly coincide with the contours of $K_{IC}/\sqrt{E_f \Gamma} = 10.0, 12.0$, and 13.0 in Fig. 11(a), respectively. It is suggested that the combined parameter, $K_{IC}/\sqrt{E_f \Gamma}$, could be approximately used to characterize the buckling modes transition. The dependence of the buckling mode on $K_{IC}/\sqrt{E_f \Gamma}$ at different λ and η is shown in Fig. 11(b). The transition in buckle morphology from rectangular to triangular and the transition in condition from cracked to uncracked can be quantitatively assessed by using the mechanical properties of K_{IC} , E_f and Γ . This correlation will be helpful for controlling the buckling behaviors through artificially tuning the modulation structure of the NMFs.

Finally, the possible effect of residual stress on the cracking and buckling behaviors of NMFs is discussed. It is generally accepted that residual tensile stress will favor the formation of straight cracks whereas compressive residual stress will tend to promote buckling in single layer films [89,90]. In the present work, the residual tensile stresses in NMFs are experimentally found to vary markedly with λ at $\eta = 1.0$ (Fig. 2(b)). However, all of the NMFs display straight cracks regardless of λ at $\eta = 1.0$ (Fig. 4). In contrast, the residual stresses in NMFs are nearly unchangeable with η (Fig. 2(c)). While a transition from straight cracks to zigzag cracks is clearly observed with decreasing η , which is a common finding at both $\lambda = 25$ and 50 nm (Fig. 4). Similarly, the buckling mode is independent of λ at $\eta = 1.0$ (Fig. 5), but strongly dependent on η at both $\lambda = 25$ and 50 nm (Fig. 5). These results evidently demonstrate that in the present NMFs, length-scale-dependent cracking and buckling behaviors are not predominantly caused by the residual stress but by a constraining effect between the two constraint layers, as we proposed in this manuscript. In addition, we can understand this conclusion from another point of view. In the NMFs composed of brittle Cr layers and soft Cu layers, the microcracks first initiate within, and subsequently run across, the Cr layers, mainly because the Cr layers with lower ductilities have more difficulty accommodating the strain [59]. Based on this consideration, the relatively high residual tensile stresses in the Cr layers will accelerate the microcrack nucleation. Further propagation of the microcracks in the NMFs is highly controlled by the constraining effect of the Cu layers [59]. This means the residual stress may

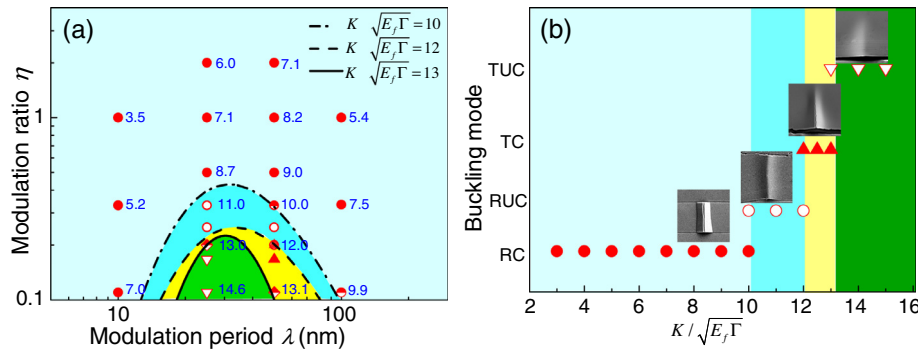


Fig. 11. (a) shows experimental $K_{IC}/\sqrt{E_f \Gamma}$ contours as functions of λ and η . (b) Dependence of buckling mode on $K_{IC}/\sqrt{E_f \Gamma}$ at different λ and η . The insets are corresponding SEM images of buckles showing typically the four types of buckling modes, respectively.

strongly impact the fracturing of Cr films but plays only a minor role in the fracturing of the whole NMFs. The effect of the residual tensile stresses on buckling has been discussed in a previous study of Cr films [13], where it was suggested that the residual stresses, even on the order of 1 GPa, played a negligible role in the transverse buckling.

5. Conclusions

- (1) Length-scale-dependent cracking behaviors have been found when stretching Cu/Cr NMFs. A cracking map with λ and η as axes was constructed, and two regimes could be identified. One is brittle fracturing with straight cracks and the other is ductile fracturing with zigzag cracks. The ductile fracture regime is located within the narrow domain of $\lambda \sim 40 \pm 20$ nm and simultaneously $\eta < \sim 0.3$, and the brittle-to-ductile transition is characterized by a fracture toughness criterion of $K_{IC} \sim 12.5$ MPa m $^{1/2}$.
- (2) The buckling behaviors were also found to be length scale dependent. A buckling map was also constructed. Four regimes are distinguished in the buckling map, i.e., cracked rectangular buckles, uncracked rectangular buckles, cracked triangular buckles, and uncracked triangular buckles. The effects of the length-scale-dependent deformation and adhesion energy on the buckling behaviors were discussed.
- (3) The critical cracking strain, critical buckling strain and fracture toughness of the Cu/Cr NMFs were experimentally measured. A modified energy balance model was proposed to evaluate the adhesion energy of the NMFs using the buckle dimensions. All of the mechanical properties are strongly dependent on the modulation period and modulation ratio. In particular, the fracture toughness can be used to characterize the cracking behaviors and the fracture toughness contour of 12.5 MPa m $^{1/2}$ outlines the transition in fracture regime from brittle to ductile. A combined parameter of $K_{IC}/\sqrt{E_f \Gamma}$ was proposed to assess the buckling behaviors, and the contours of $K_{IC}/\sqrt{E_f \Gamma}$ corresponded well to the boundaries dividing the four buckling regimes.

Acknowledgments

This work was supported by the National Natural Science Foundation of China (Grant Nos. 51321003, 51322104, 51201123 and 51571157), the 973 Program of China (Grant No. 2010CB631003), and the 111 Project of China (B06025). GL is grateful for the support from the Fundamental Research Funds for the Central Universities and the Tengfei Scholar project. JYZ thanks China

Postdoctoral Science Foundation (2012M521765), Natural Science Basic Research Plan in Shaanxi Province of China (Program No. 2015JM5158) and Shaanxi Province Postdoctoral Scientific Research Projects for part of financial support.

References

- [1] H.O. Jacobs, A.R. Tao, A. Schwartz, D.H. Gracias, G.M. Whitesides, Fabrication of a cylindrical display by patterned assembly, *Science* 296 (2002) 323–325.
- [2] J.A. Rogers, T. Someya, Y. Huang, Materials and mechanics for stretchable electronics, *Science* 327 (2010) 1603–1607.
- [3] J.A. Rogers, Z. Bao, K. Baldwin, A. Dodabalapur, B. Crone, V.R. Raju, V. Kuck, H. Katz, K. Amundson, J. Ewing, P. Drzaic, Paper-like electronic displays: large-area rubber-stamped plastic sheets of electronics and microencapsulated electrophoretic inks, *Proc. Natl. Acad. Sci.* 98 (2001) 4835–4840.
- [4] M.B. Schubert, J.H. Werner, Flexible solar cells for clothing, *Mater. Today* 9 (2006) 42–50.
- [5] T. Someya, T. Sekitani, S. Iba, Y. Kato, H. Kawaguchi, T. Sakurai, A large-area, flexible pressure sensor matrix with organic field-effect transistors for artificial skin applications, *Proc. Natl. Acad. Sci.* 101 (2004) 9966–9970.
- [6] I. Graz, M. Kaltenbrunner, C. Keplinger, R. Schwödauer, S. Bauer, S.P. Lacour, S. Wagner, Flexible ferroelectric field-effect transistor for large-area sensor skins and microphones, *Appl. Phys. Lett.* 89 (2006) 073501.
- [7] D.-Y. Khang, H. Jiang, Y. Huang, J.A. Rogers, A stretchable form of single-crystal silicon for high-performance electronics on rubber substrates, *Science* 311 (2006) 208–212.
- [8] H. Jiang, Y. Sun, J.A. Rogers, Y. Huang, Mechanics of precisely controlled thin film buckling on elastomeric substrate, *Appl. Phys. Lett.* 90 (2007) 133119.
- [9] Y. Sun, W.M. Choi, H. Jiang, Y.Y. Huang, J.A. Rogers, Controlled buckling of semiconductor nanoribbons for stretchable electronics, *Nat. Nanotechnol.* 1 (2006) 201–207.
- [10] H.C. Ko, M.P. Stoykovich, J. Song, V. Malyarchuk, W.M. Choi, C.-J. Yu, J.B. Geddes III, J. Xiao, S. Wang, Y. Huang, J.A. Rogers, A hemispherical electronic eye camera based on compressible silicon optoelectronics, *Nature* 454 (2008) 748–753.
- [11] Y. Qi, J. Kim, T.D. Nguyen, B. Lisko, P.K. Purohit, M.C. McAlpine, Enhanced piezoelectricity and stretchability in energy harvesting devices fabricated from buckled PZT ribbons, *Nano Lett.* 11 (2011) 1331–1336.
- [12] N. Matuda, S. Baba, A. Kinbara, Internal stress, young's modulus and adhesion energy of carbon films on glass substrates, *Thin Solid Films* 81 (1981) 301–305.
- [13] M.J. Cordill, F.D. Fischer, F.G. Rammerstorfer, G. Dehm, Adhesion energies of Cr thin films on polyimide determined from buckling: experiment and model, *Acta Mater.* 58 (2010) 5520–5531.
- [14] A. Pundt, E. Nikitin, P. Pekarski, R. Kirchheim, Adhesion energy between metal films and polymers obtained by studying buckling induced by hydrogen, *Acta Mater.* 52 (2004) 1579–1587.
- [15] C. Coupeau, From thin film and coating buckling structures to mechanical properties, *Mater. Sci. Eng., A* 483 (2008) 617–619.
- [16] J.W. Hutchinson, Z. Suo, Mixed mode cracking in layered materials, *Adv. Appl. Mech.* 29 (1992) 191.
- [17] M.W. Moon, H.M. Jensen, J.W. Hutchinson, K.H. Oh, A.G. Evans, The characterization of telephone cord buckling of compressed thin films on substrates, *J. Mech. Phys. Solids* 50 (2002) 2355–2377.
- [18] M.W. Moon, K.R. Lee, K.H. Oh, J.W. Hutchinson, Buckle delamination on patterned substrates, *Acta Mater.* 52 (2004) 3151–3159.
- [19] M.J. Cordill, D.F. Bahr, N.R. Moody, W.W. Gerberich, Adhesion measurements using telephone cord buckles, *Mater. Sci. Eng., A* 443 (2007) 150–155.
- [20] A.A. Abdallah, D. Kozodaev, P.C.P. Bouten, J.M.J. den Toonder, U.S. Schubert, G. de With, Buckle morphology of compressed inorganic thin layers on a polymer substrate, *Thin Solid Films* 503 (2006) 167–176.

- [21] A.A. Abdallah, P.C.P. Bouten, G. de With, Experimental study on buckle evolution of thin inorganic layers on a polymer substrate, *Eng. Fract. Mech.* 77 (2010) 2896–2905.
- [22] G. Parry, C. Coupeau, J. Colin, A. Cimetière, J. Grilhé, Buckling and post-buckling of stressed straight-sided wrinkles: experimental AFM observations of bubbles formation and finite element simulations, *Acta Mater.* 52 (2004) 3959–3966.
- [23] C.M. Stafford, C. Harrison, K.L. Beers, A. Karim, E.J. Amis, M.R. VanLandingham, H.-C. Kim, W. Volksen, R.D. Miller, E.E. Simonyi, A buckling-based metrology for measuring the elastic moduli of polymeric thin films, *Nat. Mater.* 3 (2004) 545–550.
- [24] S. Tarasovs, J. Andersons, Y. Leterrier, Estimation of interfacial fracture toughness based on progressive edge delamination of a thin transparent coating on a polymer substrate, *Acta Mater.* 58 (2010) 2948–2956.
- [25] S. Frank, U.A. Hande, S. Olliges, R. Spolenak, The relationship between thin film fragmentation and buckle formation: synchrotron-based *in situ* studies and two-dimensional stress analysis, *Acta Mater.* 57 (2009) 1442–1453.
- [26] F. Toth, F.G. Rammerstorfer, M.J. Cordill, F.D. Fischer, Detailed modelling of delamination buckling of thin films under global tension, *Acta Mater.* 61 (2013) 2425–2433.
- [27] H. Jin, W.Y. Lu, M.J. Cordill, K. Schmidegg, In situ study of cracking and buckling of chromium films on PET substrates, *Exp. Mech.* 51 (2011) 219–227.
- [28] D. Bernoulli, K. Häfliger, K. Thorwarth, G. Thorwarth, R. Hauert, R. Spolenak, Cohesive and adhesive failure of hard and brittle films on ductile metallic substrates: a film thickness size effect analysis of the model system hydrogenated diamond-like carbon (a-C:H) on Ti substrates, *Acta Mater.* 83 (2015) 29–36.
- [29] B.-J. Kim, H.-A.S. Shin, S.-Y. Jung, Y. Cho, O. Kraft, I.-S. Choi, Y.-C. Joo, Crack nucleation during mechanical fatigue in thin metal films on flexible substrates, *Acta Mater.* 61 (2013) 3473–3481.
- [30] T. Li, Z. Suo, Ductility of thin metal films on polymer substrates modulated by interfacial adhesion, *Int. J. Solids Struct.* 44 (2007) 1696–1705.
- [31] N. Lu, Z. Suo, J.J. Vlassak, The effect of film thickness on the failure strain of polymer-supported metal films, *Acta Mater.* 58 (2010) 1679–1687.
- [32] S. Frank, P.A. Gruber, U.A. Hande, R. Spolenak, In situ studies on the cohesive properties of α - and β -Ta layers on polyimide substrates, *Acta Mater.* 59 (2011) 5881–5892.
- [33] B. Erdem Alaca, M.T.A. Saif, H. Sehitoglu, On the interface debond at the edge of a thin film on a thick substrate, *Acta Mater.* 50 (2002) 1197–1209.
- [34] M. Hommel, O. Kraft, Deformation behavior of thin copper films on deformable substrates, *Acta Mater.* 49 (2001) 3935–3947.
- [35] Z. Jia, C. Peng, J. Lou, T. Li, A map of competing buckling-driven failure modes of substrate-supported thin brittle films, *Thin Solid Films* 520 (2012) 6576–6580.
- [36] H.-J. Kim, M.-W. Moon, D.-L. Kim, K.-R. Lee, K.H. Oh, Observation of the failure mechanism for diamond-like carbon film on stainless steel under tensile loading, *Scr. Mater.* 57 (2007) 1016–1019.
- [37] J. Colin, C. Coupeau, J. Grilhé, Plastic folding of buckling structures, *Phys. Rev. Lett.* 99 (2007) 046101.
- [38] J. Durinck, C. Coupeau, J. Colin, J. Grilhe, Molecular dynamics simulations of buckling-induced plasticity, *Appl. Phys. Lett.* 93 (2008) 221904.
- [39] J. Durinck, C. Coupeau, J. Colin, J. Grilhe, A stress relaxation mechanism through buckling-induced dislocations in thin films, *J. Appl. Phys.* 108 (2010) 026104.
- [40] J. Wang, A. Misra, An overview of interface-dominated deformation mechanisms in metallic multilayers, *Curr. Opin. Solid State Mater. Sci.* 15 (2011) 20–28.
- [41] M.A. Phillips, B.M. Clemens, W.D. Nix, A model for dislocation behavior during deformation of Al/Al₃Sc (fcc/L1₂) metallic multilayers, *Acta Mater.* 51 (2003) 3157–3170.
- [42] G.S. Was, T. Foecke, Deformation and fracture in microlaminates, *Thin Solid Films* 286 (1996) 1–31.
- [43] N. Mara, I. Beyerlein, Review: effect of bimetal interface structure on the mechanical behavior of Cu-Nb fcc-bcc nanolayered composites, *J. Mater. Sci.* 49 (2014) 6497–6516.
- [44] I.J. Beyerlein, J.R. Mayeur, Mesoscale investigations for the evolution of interfaces in plasticity, *Curr. Opin. Solid State Mater. Sci.* 19 (2015) 203–211.
- [45] J. Wang, R.G. Hoagland, J.P. Hirth, A. Misra, Atomistic modeling of the interaction of glide dislocations with “weak” interfaces, *Acta Mater.* 56 (2008) 5685–5693.
- [46] A. Misra, J.P. Hirth, R.G. Hoagland, Length-scale-dependent deformation mechanisms in incoherent metallic multilayered composites, *Acta Mater.* 53 (2005) 4817–4824.
- [47] J.Y. Zhang, S. Lei, Y. Liu, J.J. Niu, Y. Chen, G. Liu, X. Zhang, J. Sun, Length scale-dependent deformation behavior of nanolayered Cu/Zr micropillars, *Acta Mater.* 60 (2012) 1610–1622.
- [48] D. Bhattacharya, N.A. Mara, P. Dickerson, R.G. Hoagland, A. Misra, Compressive flow behavior of Al-TiN multilayers at nanometer scale layer thickness, *Acta Mater.* 59 (2011) 3804–3816.
- [49] I.J. Beyerlein, M.J. Demkowicz, A. Misra, B.P. Uberuaga, Defect-interface interactions, *Prog. Mater Sci.* 74 (2015) 125–210.
- [50] J.Y. Zhang, X. Zhang, R.H. Wang, S.Y. Lei, P. Zhang, J.J. Niu, G. Liu, G.J. Zhang, J. Sun, Length-scale-dependent deformation and fracture behavior of Cu/X (X = Nb, Zr) multilayers: the constraining effects of the ductile phase on the brittle phase, *Acta Mater.* 59 (2011) 7368–7379.
- [51] I. Knorr, N.M. Cordero, E.T. Lilleodden, C.A. Volkert, Mechanical behavior of nanoscale Cu/PdSi multilayers, *Acta Mater.* 61 (2013) 4984–4995.
- [52] Y. Chen, Y. Liu, C. Sun, K.Y. Yu, M. Song, H. Wang, X. Zhang, Microstructure and strengthening mechanisms in Cu/Fe multilayers, *Acta Mater.* 60 (2012) 6312–6321.
- [53] Y. Liu, D. Bufford, H. Wang, C. Sun, X. Zhang, Mechanical properties of highly textured Cu/Ni multilayers, *Acta Mater.* 59 (2011) 1924–1933.
- [54] X. Zhang, A. Misra, Residual stresses in sputter-deposited copper/330 stainless steel multilayers, *J. Appl. Phys.* 96 (2004) 7173–7178.
- [55] A. Misra, H. Kung, T.E. Mitchell, M. Nastasi, Residual stresses in polycrystalline Cu/Cr multilayered thin films, *J. Mater. Res.* 15 (2000) 756–763.
- [56] A.L. Shull, F. Spaepen, Measurements of stress during vapor deposition of copper and silver thin films and multilayers, *J. Appl. Phys.* 80 (1996) 6243–6256.
- [57] L.B. Freund, S. Suresh, *Thin Film Materials: Stress, Defect Formation and Surface Evolution*, Cambridge University Press, 2004.
- [58] J.Y. Zhang, X. Zhang, G. Liu, G.J. Zhang, J. Sun, Scaling of the ductility with yield strength in nanostructured Cu/Cr multilayer films, *Scr. Mater.* 63 (2010) 101–104.
- [59] J.Y. Zhang, G. Liu, X. Zhang, G.J. Zhang, J. Sun, E. Ma, A maximum in ductility and fracture toughness in nanostructured Cu/Cr multilayer films, *Scr. Mater.* 62 (2010) 333–336.
- [60] R.M. Niu, G. Liu, C. Wang, G. Zhang, X.D. Ding, J. Sun, Thickness dependent critical strain in submicron Cu films adherent to polymer substrate, *Appl. Phys. Lett.* 90 (2007) 161907–161907.
- [61] L.B. Freund, E. Chason, Model for stress generated upon contact of neighboring islands on the surface of a substrate, *J. Appl. Phys.* 89 (2001) 4866–4873.
- [62] R.W. Hoffman, Stresses in thin films: the relevance of grain boundaries and impurities, *Thin Solid Films* 34 (1976) 185–190.
- [63] W.D. Nix, B.M. Clemens, Crystallite coalescence: a mechanism for intrinsic tensile stresses in thin films, *J. Mater. Res.* 14 (1999) 3467–3473.
- [64] F. Spaepen, Interfaces and stresses in thin films, *Acta Mater.* 48 (2000) 31–42.
- [65] H. Windischmann, Intrinsic stress in sputter-deposited thin films, *Crit. Rev. Solid State Mater. Sci.* 21 (1992) 547–596.
- [66] M.J. Cordill, A. Taylor, J. Schalko, G. Dehm, Fracture and delamination of chromium thin films on polymer substrates, *Mettal. Mater. Trans. A* 41 (2010) 870–875.
- [67] M. Janda, On the intrinsic stress in thin chromium films, *Thin Solid Films* 142 (1986) 37–45.
- [68] D.W. Hoffman, J.A. Thornton, Internal stresses in sputtered chromium, *Thin Solid Films* 40 (1977) 355–363.
- [69] A. Misra, M. Nastasi, Evolution of tensile residual stress in thin metal films during energetic particle deposition, *J. Mater. Res.* 14 (1999) 4466–4469.
- [70] G.C.A.M. Janssen, A.J. Dammers, V.G.M. Sivel, W.R. Wang, Tensile stress in hard metal films, *Appl. Phys. Lett.* 83 (2003) 3287–3289.
- [71] A. Misra, S. Fayeulle, H. Kung, T.E. Mitchell, M. Nastasi, Residual stresses and ion implantation effects in Cr thin films, *Nucl. Instrum. Methods B* 148 (1999) 211–215.
- [72] J.A. Thornton, D.W. Hoffman, Stress-related effects in thin films, *Thin Solid Films* 171 (1989) 5–31.
- [73] G.C.A.M. Janssen, Stress and strain in polycrystalline thin films, *Thin Solid Films* 515 (2007) 6654–6664.
- [74] C.C. Aydiner, D.W. Brown, A. Misra, N.A. Mara, Y.-C. Wang, J.J. Wall, J. Almer, Residual strain and texture in free-standing nanoscale Cu-Nb multilayers, *J. Appl. Phys.* 102 (2007) 083514.
- [75] R. Su, L. Li, Z.H. Nie, Q.H. Zhang, Y.D. Wang, X.T. Zhou, Y.D. Wu, X.D. Hui, X.J. Li, M.G. Wang, Interface stress development in the Cu/Ag nanostructured multilayered film during the tensile deformation, *Appl. Phys. Lett.* 105 (2014) 221907.
- [76] M. Stefenelli, R. Daniel, W. Ecker, D. Kiener, J. Todt, A. Zeilinger, C. Mitterer, M. Burghammer, J. Keckes, X-ray nanodiffraction reveals stress distribution across an indented multilayered CrN-Cr thin film, *Acta Mater.* 85 (2015) 24–31.
- [77] H.-C. Seo, I. Petrov, H. Jeong, P. Chapman, K. Kim, Elastic buckling of AlN ribbons on elastomeric substrate, *Appl. Phys. Lett.* 94 (2009) 092104.
- [78] K. Wu, J.Y. Zhang, G. Liu, P. Zhang, P.M. Cheng, J. Li, G.J. Zhang, J. Sun, Buckling behaviors and adhesion energy of nanostructured Cu/X (X = Nb, Zr) multilayer films on a compliant substrate, *Acta Mater.* 61 (2013) 7889–7903.
- [79] K.J. Hsia, Z. Suo, W. Yang, Cleavage due to dislocation confinement in layered materials, *J. Mech. Phys. Solids* 42 (1994) 877–896.
- [80] R.W. Hertzberg, *Deformation and Fracture Mechanics of Engineering Materials*, Wiley, New York, 1996.
- [81] M. Lane, R.H. Dauskardt, A. Vainchtein, H. Gao, Plasticity contributions to interface adhesion in thin-film interconnect structures, *J. Mater. Res.* 15 (2000) 2758–2769.
- [82] H.F. Wang, W.W. Gerberich, C.J. Skowronek, Fracture mechanics of Ti/Al₂O₃ interfaces, *Acta Metall. Mater.* 41 (1993) 2425–2432.
- [83] N.R. Moody, D.P. Adams, D. Medlin, T. Headley, N. Yang, A. Volinsky, Effects of diffusion on interfacial fracture of gold-chromium hybrid microcircuit films, *Int. J. Fract.* 120 (2003) 407–419.
- [84] W.W. Gerberich, M.J. Cordill, Physics of adhesion, *Rep. Prog. Phys.* 69 (2006) 2157.
- [85] A.A. Volinsky, N.R. Moody, W.W. Gerberich, Interfacial toughness measurements for thin films on substrates, *Acta Mater.* 50 (2002) 441–466.
- [86] H.W. Choi, K.-R. Lee, R. Wang, K.H. Oh, Fracture behavior of diamond-like carbon films on stainless steel under a micro-tensile test condition, *Diam. Relat. Mater.* 15 (2006) 38–43.

- [87] A.A. Taylor, M.J. Cordill, L. Bowles, J. Schalko, G. Dehm, An elevated temperature study of a Ti adhesion layer on polyimide, *Thin Solid Films* 531 (2013) 354–361.
- [88] B.A. Latella, G. Triani, Z. Zhang, K.T. Short, J.R. Bartlett, M. Ignat, Enhanced adhesion of atomic layer deposited titania on polycarbonate substrates, *Thin Solid Films* 515 (2007) 3138–3145.
- [89] E. Chason, A kinetic analysis of residual stress evolution in polycrystalline thin films, *Thin Solid Films* 526 (2012) 1–14.
- [90] A.J. Detor, A.M. Hodge, E. Chason, Y. Wang, H. Xu, M. Conyers, A. Nikroo, A. Hamza, Stress and microstructure evolution in thick sputtered films, *Acta Mater.* 57 (2009) 2055–2065.